

## Article

# The Pore Microstructure Evolution and Porous Properties of Large Capillary Pressure Wicks Sintered with Carbonyl Nickel Powder

Fengshi Zheng<sup>1,2,3</sup>, Linshan Wang<sup>1,2,3,4,\*</sup>, Rui Wang<sup>1,2,3</sup>, Jianwei Wang<sup>1,2,3,4</sup> , Shaoming Zhang<sup>5</sup>, Qiang Hu<sup>1,2,3,4</sup> and Limin Wang<sup>1,2,3,4</sup>

<sup>1</sup> Metal Powder Materials Industrial Technology Research Institute of GRINM, Beijing 101407, China

<sup>2</sup> GRIPM Advanced Materials Co., Ltd., Beijing 101407, China

<sup>3</sup> General Research Institute for Nonferrous Metals, Beijing 100088, China

<sup>4</sup> Beijing GRIPM Advanced Materials Research Institute Co., Ltd., Beijing 101407, China

<sup>5</sup> China Iron & Steel Research Institute Group, Beijing 100081, China

\* Correspondence: wls@gripm.com

**Abstract:** We investigated the effect of different sintering temperatures ranging from 200 °C to 600 °C on the porous properties and pore microstructure of large capillary pressure wicks made of carbonyl nickel powder. The evolution model of hydraulic diameter was established and verified by the maximum pore diameter. Hydraulic diameter changed as the roughness of particle surfaces decreased and sintering necks grew large during sintering. In the contact-formation stage and the initial sintering stage (200–500 °C), the decrease in the roughness of particle surfaces played a decisive role, contributing to an increase in hydraulic diameter. In the intermediate sintering stage (600 °C), the growth of sintering necks dominated the process, however the hydraulic diameter was reduced. These results show that the maximum pore diameter first increased and then decreased in the same way as our evolution model. Permeability and capillary performance of the wicks first increased and then declined with increasing sintering temperature. We found the optimal sintering temperature to be 400 °C, at which point the wicks achieved the maximum pore diameter of 1.21 μm, a permeability of  $1.77 \times 10^{-14} \text{ m}^2$ , and their highest capillary performance of  $1.46 \times 10^{-8} \text{ m}$ .

**Keywords:** wicks; carbonyl nickel powder; sintering temperature; maximum pore diameter; permeability



**Citation:** Zheng, F.; Wang, L.; Wang, R.; Wang, J.; Zhang, S.; Hu, Q.; Wang, L. The Pore Microstructure Evolution and Porous Properties of Large Capillary Pressure Wicks Sintered with Carbonyl Nickel Powder. *Materials* **2022**, *15*, 5830. <https://doi.org/10.3390/ma15175830>

Academic Editor: Jana Bidulská

Received: 15 July 2022

Accepted: 19 August 2022

Published: 24 August 2022

**Publisher's Note:** MDPI stays neutral with regard to jurisdictional claims in published maps and institutional affiliations.



**Copyright:** © 2022 by the authors. Licensee MDPI, Basel, Switzerland. This article is an open access article distributed under the terms and conditions of the Creative Commons Attribution (CC BY) license (<https://creativecommons.org/licenses/by/4.0/>).

## 1. Introduction

Increasingly large heat flux and high heat dissipation makes transferring the heat generated by electronic devices such as central processing units and hard disk drives difficult [1]. Loop heat pipes (LHPs) have attracted attention as one possible solution to this problem due to their long-distance heat transferring capabilities, flexible configurations, various possible working orientations, and ability to transfer heat in systems with only small temperature differences [2–4]. The wick inside LHPs, a kind of porous material, is considered the most important component since it provides capillary pressure to circulate the working fluid inside a closed loop where no external power is required, and capillary pressure and permeability are the key parameters of wicks [1]. To optimize their capillary performance, high permeability and powerful capillary pressure are typically needed. However, there is always a tradeoff between permeability and capillary pressure. A smaller pore size increases the capillary pressure of a wick; however, the smaller the pore size is, the lower the permeability is [5]. Considering this tradeoff, wicks are generally divided into two types according to their critical features: high permeability wicks and large capillary pressure wicks. High permeability wicks usually provide LHPs with high heat flux transferring capabilities over a hundred-millimeter distance at horizontal orientation [2,3,6]. Large capillary pressure wicks ensure the efficient operation of LHPs over a thousand-millimeter distance at any orientation [6].

There are several excellent materials for wicks, such as nickel, titanium, polymeric, ceramic, copper and stainless steel, while those made of carbonyl nickel powder possess the highest purity, controllable porosity and pore size, appropriate mechanical properties, moderate thermal conductivity, and compatibility with various working fluids. Hence, carbonyl nickel powder is widely used to fabricate high-performance wicks [6–8].

To fabricate high permeability wicks with carbonyl nickel powder, pore forming agents and loose sintering processes are usually adopted, and a comparatively high sintering temperature, which is normally higher than 550 °C, is required to obtain enough strength needed in the assembly and operation of LHP in particular [8–11]. Qu et al. [12] investigated the effects of sintering temperature and sintering holding time on the thermal performance of bi-porous nickel wicks in LHPs. Their results show that the porosity and permeability of wicks continuously decrease with increasing sintering temperature from 650 °C to 800 °C, and with prolonging sintering holding time from 30 min to 60 min. Mishra et al. [8] developed nickel wicks using the tap-sintering technique and investigated the effects of sintering temperature on the porosity, permeability and mechanical strength of wicks; their results show that the porosity and permeability of wicks decline as sintering temperature increases from 550 °C to 775 °C.

In order to manufacture large capillary pressure wicks, the method of sintering after pressing carbonyl nickel powder without pore forming agents is frequently adopted. Wicks fabricated in this method are praised for their fine pores and high strength, although their porosity and permeability are somewhat low. For LHPs, the maximum pore diameter in wicks is vitally important because there is backflow of vapor from the evaporation zone to the compensation chamber through the pore with the largest diameter due to the inverse dependence of capillary pressure on pore diameter [9]. This kind of wick is usually characterized by a porosity of around 50% and a maximum pore diameter of about 1.0  $\mu\text{m}$  [13–19]. Although this kind of wick is widely used and exhibits excellent performance, few studies have focused on the fabrication processes of this kind of wick, and its optimal sintering temperature is still unknown.

Sintering processes significantly affect the pore structure and properties of porous materials. In sintering processes, sintering necks form and grow large between particles while porosity and permeability simultaneously decrease [20]. Initially, pores in green porous materials are irregular. As sintering progresses, however, the angular pores form a smooth, near-cylindrical network with little change in pore size [20]. With increasing sintering temperature, the permeability of porous materials usually decreases, and pore size rarely changes or slightly decreases [21,22]. However, early studies have shown that the permeability and pore size of porous materials both increase with sintering temperature [23–27]. Some of these results are attributed to the liquid phase during sintering [25–27]. However, other studies have been conducted using the solid-state sintering method, and the reason for the increase in permeability and pore size remains unknown.

Lunin and Kostornov [24] made cylindrical specimens with a porosity of 50% by compacting carbonyl nickel powder, and studied the change in pore diameter distribution while sintering at different temperatures. Their results show that the mean statistical pore diameter first increases and then declines as the sintering temperature increased from 200 °C to 900 °C. Nevertheless, few researchers have studied the change in maximum pore diameter and permeability of porous materials made of carbonyl nickel powder while sintering at different temperatures. In addition, the evolution of the pore size has not been rigorously described.

In this work, we fabricated large capillary pressure wicks with carbonyl nickel powder by cold isostatic pressing followed by sintering, and studied the effects of sintering temperature on their hydraulic diameter, permeability and capillary performance. In order to analyze the changes in permeability and hydraulic diameter, the porosity and volume-specific surface area were determined, and we then investigated the fracture morphology and cross-section morphology of the wicks. Additionally, we established an evolution model of hydraulic diameter and validated it using the parameter of maximum pore diame-

ter. This work promotes understanding of the increase in pore size and permeability during sintering carbonyl nickel powder, and also provides insight into methods of fabrication for large capillary pressure wicks at an optimal sintering temperature.

## 2. Materials and Methods

Commercial carbonyl nickel powder with a mean diameter of  $1.78 \mu\text{m}$  was chosen as the raw material, and its bulk density was  $0.35 \text{ g}\cdot\text{cm}^{-3}$ . Figure 1 shows the experimental procedure in this study. Uniform green bars were first fabricated by cold isostatic pressing at 100 MPa. Then, the green bars were cut into green slices with a diameter of 25 mm and a thickness of 3.5 mm on a lathe. Finally, the green slices were sintered in a tube furnace, and the wicks were prepared. The sintering process was conducted for 3 h in a vacuum below  $1.0 \times 10^{-2} \text{ Pa}$ . The sintering temperatures ranged from  $200 \text{ }^\circ\text{C}$  to  $600 \text{ }^\circ\text{C}$  to investigate the effects of sintering temperature on the properties of wicks, and this temperature range was chosen in order to avoid large sintering shrinkage and extreme porosity decrease.

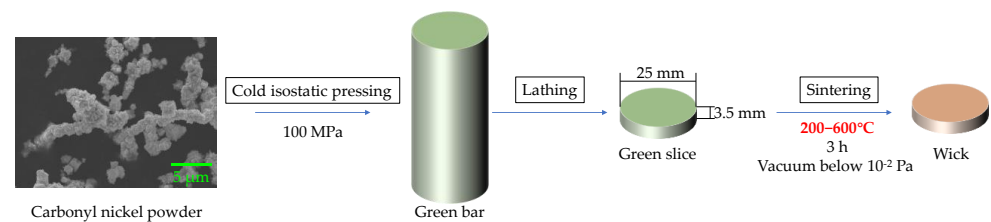


**Figure 1.** Experimental procedure.

Permeability of green slices and wicks was measured and used together with maximum pore diameter to calculate capillary performance. Digital pressure gauges with an accuracy of  $\pm 1 \text{ kPa}$  and mass flow controllers with an accuracy of  $\pm 2.5 \text{ mL}\cdot\text{min}^{-1}$  were used to determine the permeability according to ISO 4022: 2018, where nitrogen passed through samples at flow rates ranging from  $50 \text{ mL}\cdot\text{min}^{-1}$  to  $500 \text{ mL}\cdot\text{min}^{-1}$ . Absolute alcohol, nitrogen and a digital pressure gauge with an accuracy of  $\pm 1 \text{ kPa}$  were used to determine the bubble point pressure  $P_b$  of samples according to ISO 4003: 1977. The maximum pore diameter  $d_{max}$  is calculated by Equation (1):

$$d_{max} = \frac{4 \cdot \cos \theta \cdot \gamma}{P_b} \quad (1)$$

where  $\theta$  is the contact angle between absolute alcohol and samples, and  $\gamma$  is the surface tension of absolute alcohol. Radial sintering shrinkage ratio, porosity and specific surface area were measured to investigate changes in permeability. The radial sintering shrinkage ratio  $\frac{\Delta L}{L_0}$  is calculated by Equation (2):

$$\frac{\Delta L}{L_0} = \frac{L_0 - L_1}{L_0} \times 100\% \quad (2)$$

where  $L_0$  is the diameter of a green slice, and  $L_1$  is the diameter of the corresponding wick. The diameters of green slices and corresponding wicks were measured using a vernier caliper with an accuracy of  $\pm 0.01 \text{ mm}$ . According to ISO 2738: 1999, an analytical balance with an accuracy of  $\pm 0.0001 \text{ g}$  was used to determine the mass of samples  $m$  and to determine the volume of samples  $V$  by weighing the samples coated with petroleum jelly both in the air and in the water. The porosity of samples is calculated by Equation (3):

$$\varepsilon = \left(1 - \frac{m}{V \cdot \rho}\right) \times 100\% \quad (3)$$

where  $\rho$  is the true density of nickel. The surface area of samples was determined by the Brunauer–Emmett–Teller (BET) nitrogen adsorption method (Tristar plus 3030, Micromeritics Instruments Corporation, Norcross, GA, USA) according to ISO 9277: 2010, and the

volume-specific surface area was calculated by dividing surface area by the volume of samples  $V$ . At each sintering condition, 5 wicks were prepared and tested to determine these properties and characteristics. In addition, three samples with fractured surfaces and cross-sections of pores were prepared and observed using scanning electron microscopy (SEM, JSM-F100, JEOL Ltd., Tokyo, Japan).

The uncertainties for measurement of the permeability, bubble point pressure, diameter, mass and volume were estimated to be  $0.05 \times 10^{-14} \text{ m}^2$ , 1.8 kPa, 0.04 mm, 0.005 g and  $10 \text{ mm}^3$ , respectively. In addition, the relative uncertainty for measurement of the surface area was 5%. Using the standard error analysis method, the uncertainties of maximum pore diameter and radial sintering shrinkage ratio were 0.02  $\mu\text{m}$  and 0.3%, respectively, and those of porosity and volume-specific surface area were within 0.6% and  $0.18 \times 10^6 \text{ m}^{-1}$ , respectively.

### 3. Results and Discussion

#### 3.1. Evolution of Porosity and Volume-Specific Surface Area

High permeability enhances the heat transfer limit of LHPs because it reduces pressure drop of fluids while filtering through wicks during the operation of LHPs [9]. The permeability  $K$  is related to the porosity  $\epsilon$  and volume-specific surface area  $S$  by the Kozeny–Carman equation:

$$K = \frac{\epsilon^3}{C \cdot S^2} \quad (4)$$

where  $C$  is an empirical constant that depends on the material and fabrication process. Hence, porosity and volume-specific surface area are important characteristics for wick performance.

##### 3.1.1. Porosity

Figure 2 shows the porosity and radial sintering shrinkage ratio of green slices and wicks sintered at different temperatures. As we can see, the radial sintering shrinkage ratio increased while the porosity decreased with increasing sintering temperature. A large sintering shrinkage ratio of a wick meant great reductions in both its dimensions and volume in sintering, which caused a huge decrease in its porosity, considering its mass remains unchanged in sintering. Related to the small radial sintering shrinkage at 200 °C and 300 °C, the porosity of wicks showed little change compared to the porosity of the green slices, which was 49.2%. When the wicks were sintered at 400 °C, the radial shrinkage ratio slightly increased to 1.0%, hence the porosity slightly decreased to 47.5%. As the sintering temperature rose to 500 °C, the radial sintering shrinkage of the wicks evidently grew as well, so their porosity sharply dropped. At 600 °C, the radial sintering shrinkage ratio of wicks increased to 9.9%, and thus the porosity declined to 31.3%.

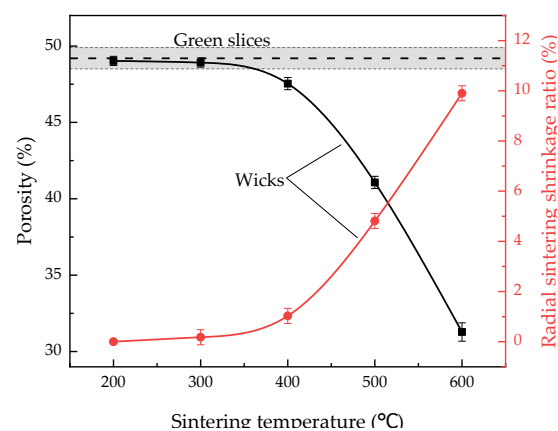


**Figure 2.** Radial shrinkage and porosity of green slices and wicks sintered at different temperatures.

Grain-boundary diffusion dominates in the sintering shrinkage of wicks in the presence of low temperatures and small particle diameters [28]. The sintering shrinkage of the

wicks in our case indicates that the grain-boundary diffusion of carbonyl nickel powder with a mean diameter of 1.78  $\mu\text{m}$  commences at 400  $^{\circ}\text{C}$ .

### 3.1.2. Volume-Specific Surface Area

Figure 3 shows the volume-specific surface area of green slices and wicks sintered at different temperatures. With increasing sintering temperature, the volume-specific surface area declined rapidly at 200–400  $^{\circ}\text{C}$  and slowly at 400–600  $^{\circ}\text{C}$ . When the wicks were sintered at 200  $^{\circ}\text{C}$ , the volume-specific surface area declined only slightly to  $3.33 \times 10^6 \text{ m}^{-1}$  compared to that of the green slices, which was  $3.67 \times 10^6 \text{ m}^{-1}$ . At 400  $^{\circ}\text{C}$ , the volume-specific surface area significantly decreased to  $2.04 \times 10^6 \text{ m}^{-1}$ . With a further increase in sintering temperature, once again only slight declines were detected in the volume-specific surface area.

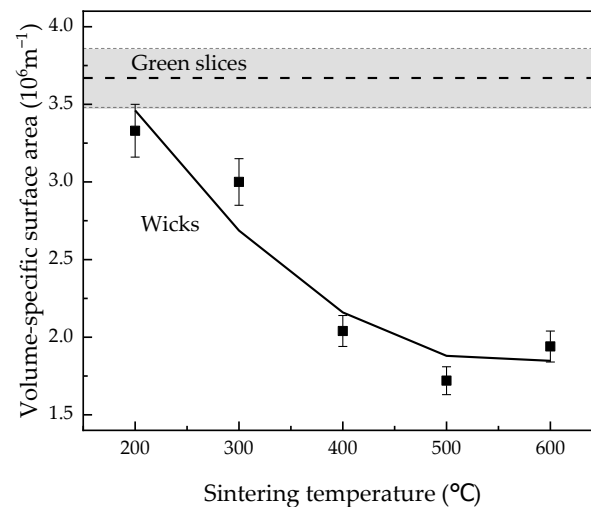


**Figure 3.** Volume-specific surface area of green slices and wicks sintered at different temperatures.

To study the change in volume-specific surface area, we observed the microstructure of green slices and wicks by SEM. Figure 4 shows the fracture morphology of a green slice and various wicks sintered at temperatures between 200  $^{\circ}\text{C}$  and 600  $^{\circ}\text{C}$ . As we can see, higher sintering temperatures led to smoother surfaces of particles and larger sintering necks between particles. Rough particle surfaces were detected in the green slice, but the increase in sintering temperature from 200  $^{\circ}\text{C}$  to 600  $^{\circ}\text{C}$  gradually smoothed the surfaces of the particles. The most pronounced decline in roughness of the particle surfaces is found at 200–400  $^{\circ}\text{C}$ .

Moreover, clear sintering necks formed between particles at 400  $^{\circ}\text{C}$  and grew larger with increasing sintering temperatures. Sintering is divided into four stages, which are the contact-formation stage where few sintering necks form, the initial stage where sintering necks grow without interaction with neighboring ones, the intermediate stage where sintering necks interact with neighboring ones, and the final stage where tubular pores pinch closed to form discrete spherical or lenticular pores [20]. As shown in Figure 4, few sintering necks were detected in wicks sintered at 200  $^{\circ}\text{C}$  and 300  $^{\circ}\text{C}$ ; sintering necks formed and grew without interaction with neighboring ones at 400  $^{\circ}\text{C}$  and 500  $^{\circ}\text{C}$ ; sintering necks interact with neighboring ones at 600  $^{\circ}\text{C}$ . Hence, sintering at 200  $^{\circ}\text{C}$  and 300  $^{\circ}\text{C}$  stopped in the contact-formation stage; sintering at 400  $^{\circ}\text{C}$  and 500  $^{\circ}\text{C}$  stopped in the initial stage; and sintering at 600  $^{\circ}\text{C}$  stopped in the intermediate stage.

Surface diffusion causes the decrease in roughness of particle surfaces, and grain-boundary diffusion together with surface diffusion contributes to the formation and growth of sintering necks. In the sintering process, atoms on rough surfaces move from a convex point to a concave point due to the chemical potential gradient introduced by the curvature gradient, leading to the decrease in roughness of particle surfaces [29]. Moreover, the final shape of the particles depends on the surface diffusion coefficient, which increases with sintering temperature [30]. As the sintering temperature increases from 200  $^{\circ}\text{C}$  to 600  $^{\circ}\text{C}$ , more atoms disperse away from convex points and accumulate at concave points due to

the increasing surface diffusion coefficient. As a result, higher sintering temperatures result in smoother particle surfaces and larger sintering necks.

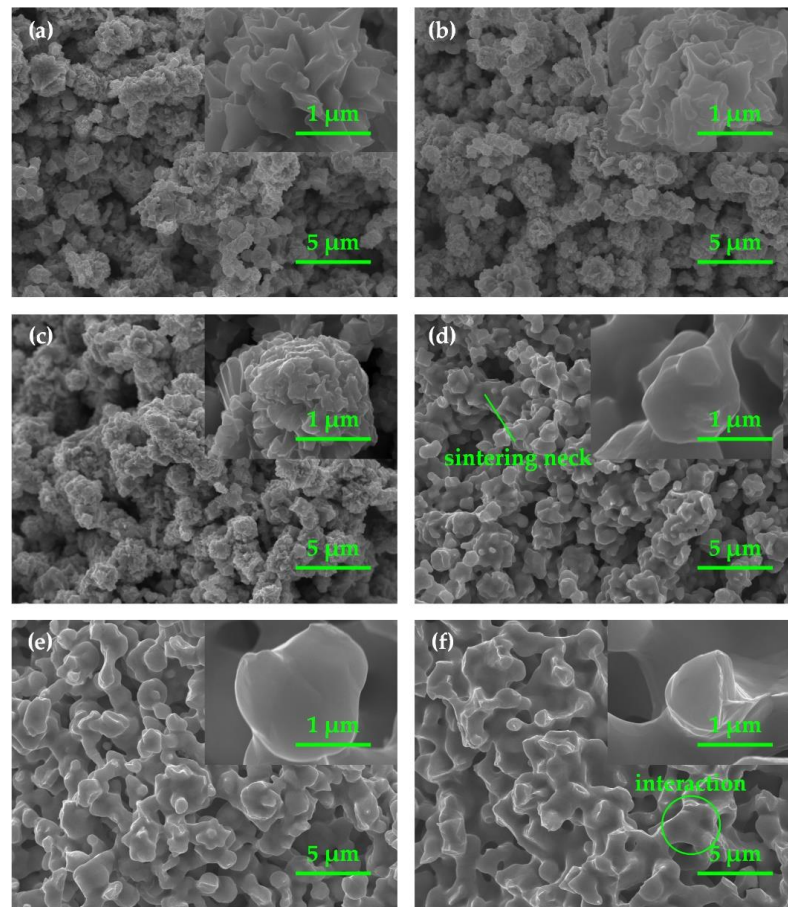


**Figure 4.** Fracture morphology of green slices and wicks sintered at different temperatures: (a) green slice, (b) 200 °C, (c) 300 °C, (d) 400 °C, (e) 500 °C, (f) 600 °C.

Grain-boundary diffusion also contributes to the growth of sintering necks. Vacant lattice points diffuse away from sintering necks and sink at the grain boundary, which results in sintering shrinkage and neck growth [31,32]. As sintering temperature increases from 400 °C to 600 °C, the grain-boundary diffusion accelerates, leading to increased sintering shrinkage and growth of sintering necks.

The decrease in roughness of particle surfaces and the growth of sintering necks together contribute to the decline in volume-specific surface area (Figure 3). The most pronounced decline in the roughness of the particle surfaces induces the volume-specific surface area to decrease significantly at 200–400 °C. Furthermore, the growth of sintering necks causes the slow decline in volume-specific surface area at 400–600 °C.

### 3.2. Evolution of Pore Size

#### 3.2.1. Evolution of Mean Pore Diameter

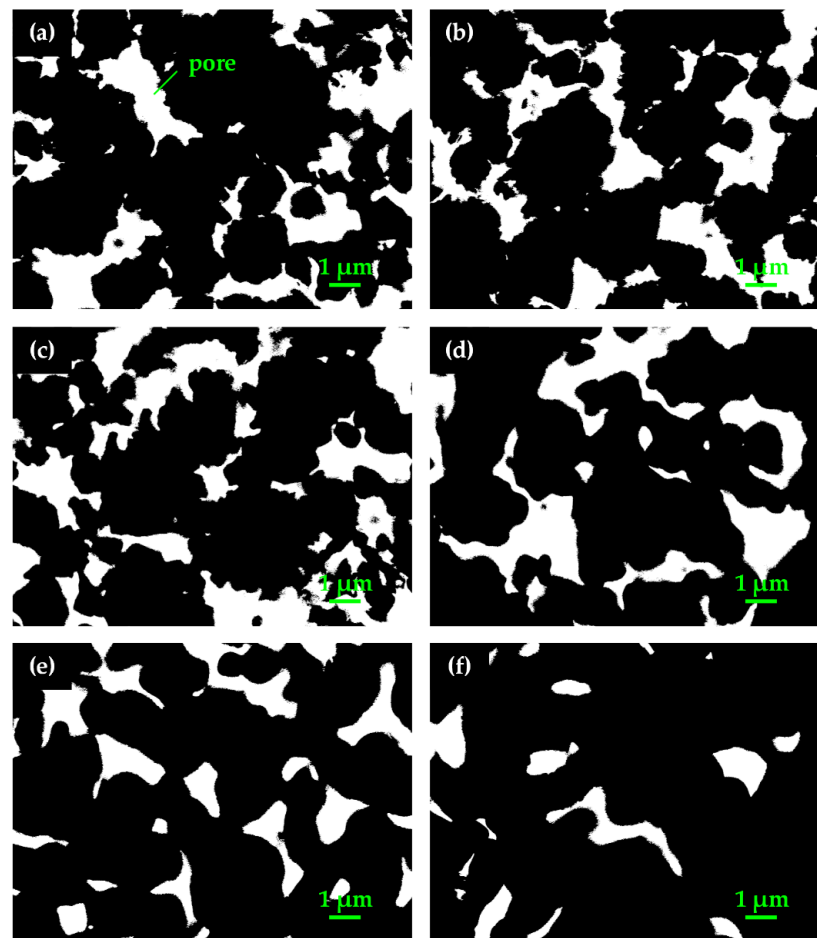
For a unique pore with an irregularly shaped cross section, the hydraulic diameter  $d_h$  of the pore at any of its cross sections is defined in Equation (5) [33] as:

$$d_h = 4 \cdot \frac{A_{pore}}{P_{pore}} \quad (5)$$

where  $A_{pore}$  is the area of the pore at the cross section, and  $P_{pore}$  is the perimeter. Countless through pores exist in porous materials, and the hydraulic diameter of every through pore varies at different cross sections. By analyzing cross-sectional images of green slices and

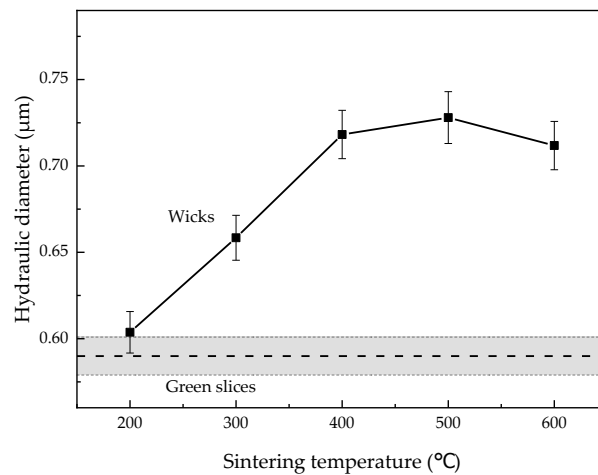
wicks, we determined the mean pore diameter that is capable of reflecting the size evolution of pores. The uncertainties for measurement of the area and perimeter were estimated to be  $0.019 \mu\text{m}^2$  and  $0.010 \mu\text{m}$ , respectively. Using the standard error analysis method, the uncertainty of the mean pore diameter was within  $0.015 \mu\text{m}$ .

Figure 5 shows the cross-section morphology of pores in green slices and wicks sintered at temperatures from  $200 \text{ }^\circ\text{C}$  to  $600 \text{ }^\circ\text{C}$ . The mean pore diameter of the green slices and wicks was determined from cross-sectional images and is shown in Figure 6. As seen in Figure 5a, the proportion of areas covered by pores is large, and the outlines of pores are zigzag in the green slice. With increasing sintering temperature, the proportional area of pores decreased, and the outlines gradually became smooth as shown in Figure 5b–f. From Figure 6, we see that the mean pore diameter first increased to the maximum at  $500 \text{ }^\circ\text{C}$ , and then declined with an increase in sintering temperature.



**Figure 5.** Cross-section morphology of pores in green slices and wicks sintered at various temperatures: (a) green slice, (b)  $200 \text{ }^\circ\text{C}$ , (c)  $300 \text{ }^\circ\text{C}$ , (d)  $400 \text{ }^\circ\text{C}$ , (e)  $500 \text{ }^\circ\text{C}$ , (f)  $600 \text{ }^\circ\text{C}$ .

The decrease in the roughness of particle surfaces (Figure 4a–f) smoothed the outlines of the pores at the cross section. With increasing sintering temperature, the roughness of particle surfaces gradually decreased, so the outlines of pores gradually became smoother. The growth of sintering necks (Figure 4d–f) reduced the proportional volume of pores in wicks. Hence, the perimeter and area of every single pore and the proportional area of pores declined at the cross section. As shown in Figure 6, the wicks sintered at  $200 \text{ }^\circ\text{C}$  and the green slices were almost the same in terms of mean pore diameter,  $0.604 \mu\text{m}$  and  $0.590 \mu\text{m}$ , respectively. When the wicks were sintered at  $300 \text{ }^\circ\text{C}$ , the roughness of the particle surfaces decreased while sintering necks formed. As a result, the perimeter of the pores declined, and the area showed little variation, resulting in an increase in the mean pore diameter.



**Figure 6.** Mean pore diameter of green slices and wicks sintered at different temperatures.

At sintering temperatures of 400 °C and 500 °C, the roughness of particle surfaces decreased significantly, and sintering necks formed and gradually grew. Additionally, the perimeter of the pores dropped faster than the area, so the mean pore diameter increased to 0.728 μm at the sintering temperature of 500 °C. As the sintering temperature further increased to 600 °C, the particle surfaces showed little change, but the sintering necks grew rapidly. Greater reduction was found in the area of pores compared to the perimeter, leading to the decline in the mean pore diameter. The change in the mean pore diameter at 600 °C indicates that the growth of sintering necks caused more reduction in the area of pores than in their perimeter.

Figure 7 summarizes the evolution of the hydraulic diameter in different sintering stages. When the wicks are sintered in the contact-formation stage (200–300 °C) and the initial sintering stage (400–500 °C), the decrease in the roughness of particle surfaces played a decisive role, contributing to an increase in hydraulic diameter. In the intermediate sintering stage (600 °C), the growth of sintering necks dominated the process, however reduced the hydraulic diameter.

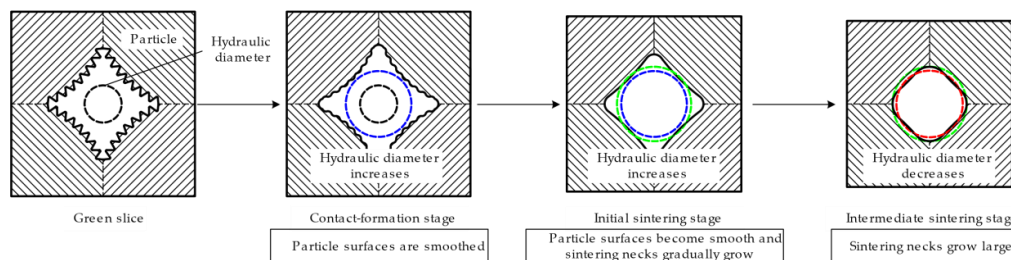


**Figure 7.** Evolution model of hydraulic diameter in different sintering stages.

### 3.2.2. Evolution of Maximum Pore Diameter

Maximum pore diameter is defined as the maximum among all the hydraulic diameters of the most constricted part in every through pore [33]. The study of maximum pore diameter is of great importance because the failures of LHPs usually commence at the pore with the largest diameter [9]. Figure 8 plots the maximum pore diameter of green slices and wicks sintered at different temperatures. As the sintering temperature increased from 200 °C to 600 °C, the maximum pore diameter first increased and then decreased in the same way as the evolution model of the hydraulic diameter (Figure 7). The wicks sintered at 400 °C and 500 °C are nearly equal in maximum pore diameter, at 1.21 μm and 1.22 μm, respectively. The experimental evolution of maximum pore diameter thus validates the evolution model of the hydraulic diameter, and this model may be applied to the pore size evolution during solid-state sintering for other particles with rough surfaces.

As seen in Figure 8, sintering at 300–600 °C always enlarges the maximum pore diameter of wicks, which is unsatisfactory. However, a sintering process is still needed to enhance the permeability and capillary performance of wicks.

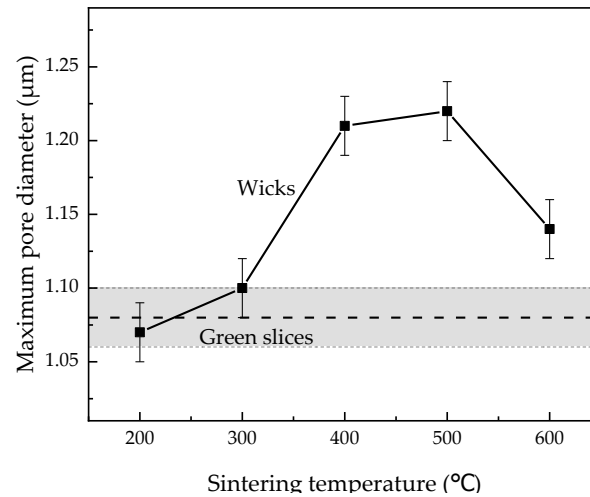


**Figure 8.** Maximum pore diameter of green slices and wicks sintered at different temperatures.

### 3.3. Porous Properties

#### 3.3.1. Permeability

Figure 9 shows the permeability and  $C$  of green slices and wicks sintered at different temperatures. With increasing sintering temperatures, the permeability of the wicks first reached the peak value of  $1.77 \times 10^{-14} \text{ m}^2$  at 400 °C, and then decreased. When the wicks were sintered at 200 °C, the volume-specific surface area (Figure 3) and the porosity (Figure 2) barely changed, resulting in similar permeability compared to the green slices. From Equation (4) and observed values of porosity, volume-specific surface area and permeability, the empirical constant  $C$  was calculated, and the uncertainty of  $C$  was within 0.11. As sintering temperature increased from 200 °C to 600 °C,  $C$  first increased and then decreased. Wicks sintered at 400 °C and 500 °C showed nearly the same values of  $C$ , which were 1.45 and 1.50, respectively.

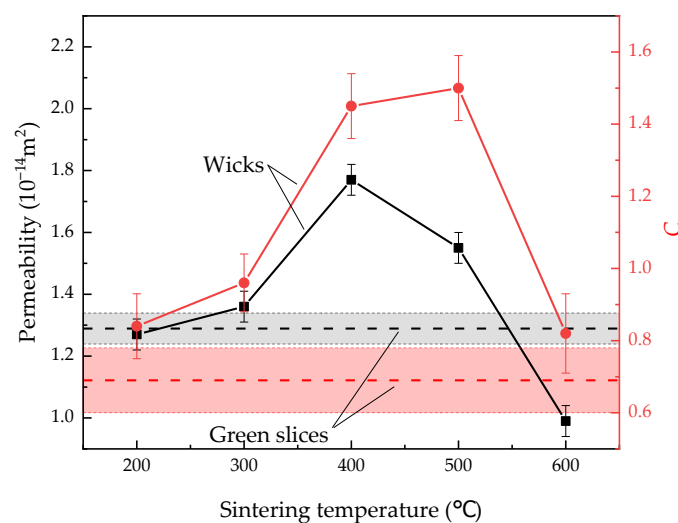


**Figure 9.** Permeability and  $C$  of green slices and wicks sintered at different temperatures.

#### 3.3.2. Capillary Performance

Capillary performance parameter is usually defined as the ratio of permeability to pore diameter [34,35]. In this study, we use the ratio of permeability to the maximum pore diameter

diameter  $K/d_{max}$  to evaluate the capillary performance of our wicks because the maximum diameter of the wicks determines the heat transfer limit of LHPs [9]. Figure 10 shows the capillary performance of green slices and wicks sintered at different temperatures, and the uncertainty of  $K/d_{max}$  was  $0.05 \times 10^{-8}$  m. The capillary performance first increased to the maximum at 400 °C, and then declined with increasing sintering temperatures. The changes in the capillary performance of the wicks show that the sintering temperature of 400 °C granted the wicks the highest capillary performance of  $1.46 \times 10^{-8}$  m. When the wicks were sintered at 400 °C, the capillary performance and the permeability increased by 23.7% and 37.5%, respectively, while the maximum pore diameter increased by 12.0% compared to the green slices.

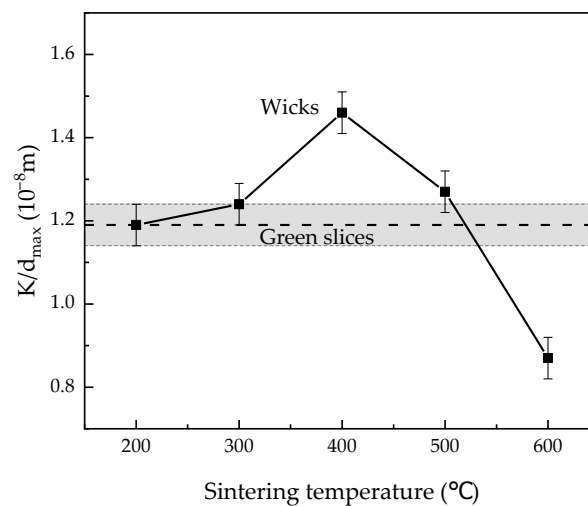


**Figure 10.** Capillary performance of green slices and wicks sintered at different temperatures.

#### 4. Conclusions

Based on the pore microstructure and porous properties of large capillary pressure wicks sintered at different temperatures, a summary is proposed:

- (1) The pore size first increased and then decreased with increasing sintering temperature from 200 °C to 600 °C. When the wicks were sintered at 400 and 500, the maximum pore diameter reached 1.21  $\mu$ m and 1.22  $\mu$ m, respectively, which were the highest levels in this study.
- (2) The evolution model of hydraulic diameter with increasing sintering temperature was established and validated. In the contact-formation stage and the initial sintering stage (200–500 °C), the decrease in the roughness of particle surfaces played a decisive role. More reduction in the perimeter compared to the area led to an increase in hydraulic diameter. In the intermediate sintering stage (600 °C), the growth of sintering necks took on a dominant role, which caused more reduction in the area than in the perimeter, leading to a decline in hydraulic diameter.
- (3) The optimal sintering temperature proved to be 400 °C, at which point the wicks achieved the permeability of  $1.77 \times 10^{-14}$  m<sup>2</sup> and their highest capillary performance of  $1.46 \times 10^{-8}$  m.

**Author Contributions:** Investigation, F.Z. and R.W.; writing—original draft, F.Z. and R.W.; visualization, F.Z.; methodology, L.W. (Linshan Wang), J.W., S.Z., Q.H. and L.W. (Limin Wang); project administration, L.W. (Linshan Wang) and S.Z.; writing—review and editing, L.W. (Linshan Wang), J.W., S.Z., Q.H. and L.W. (Limin Wang) All authors have read and agreed to the published version of the manuscript.

**Funding:** This study was supported by the National Key Research and Development Program of China (No. 2021YFB3701905).

**Institutional Review Board Statement:** Not applicable.

**Informed Consent Statement:** Not applicable.

**Data Availability Statement:** Not applicable.

**Conflicts of Interest:** The authors declare that they have no known competing financial interests or personal relationships that could have appeared to influence the work reported.

## References

1. Li, H.; Fu, S.; Li, G.; Fu, T.; Zhou, R.; Tang, Y.; Tang, B.; Deng, Y.; Zhou, G. Effect of fabrication parameters on capillary pumping performance of multiscale composite porous wicks for loop heat pipe. *Appl. Therm. Eng.* **2018**, *143*, 621–629. [[CrossRef](#)]
2. Choi, J.; Jeong, M. Preliminary design on high-end workstation cooling system using loop heat pipes. *Therm. Sci. Eng. Prog.* **2020**, *20*, 100519. [[CrossRef](#)]
3. Du, S.; Zhang, Q.; Hou, P.; Yue, C.; Zou, S. Experimental study and steady-state model of a novel plate loop heat pipe without compensation chamber for CPU cooling. *Sustain. Cities. Soc.* **2020**, *53*, 101894. [[CrossRef](#)]
4. Zhou, G.; Li, J.; Jia, Z. Power-saving exploration for high-end ultra-slim laptop computers with miniature loop heat pipe cooling module. *Appl. Energy* **2019**, *239*, 859–875. [[CrossRef](#)]
5. Dominguez Espinosa, F.A.; Peters, T.B.; Brisson, J.G. Effect of fabrication parameters on the thermophysical properties of sintered wicks for heat pipe applications. *Int. J. Heat Mass Transf.* **2012**, *55*, 7471–7486. [[CrossRef](#)]
6. Maydanik, Y.F. Loop heat pipes. *Appl. Therm. Eng.* **2005**, *25*, 635–657. [[CrossRef](#)]
7. Zhao, R.; Zhang, Z.; Zhao, S.; Cui, H.; Liu, Z.; Liu, W. Experimental study of flat-disk loop heat pipe with R1233zd(E) for cooling terrestrial electronics. *Appl. Therm. Eng.* **2021**, *197*, 117385. [[CrossRef](#)]
8. Mishra, D.K.; Saravanan, T.T.; Khanra, G.P.; Girikummar, S.; Sharma, S.C.; Sreekumar, K.; Sinha, P.P. Studies on the processing of nickel base porous wicks for capillary pumped loop for thermal management of spacecrafts. *Adv. Powder Technol.* **2010**, *21*, 658–662. [[CrossRef](#)]
9. Singh, R.; Nguyen, T.; Mochizuki, M. Capillary evaporator development and qualification for loop heat pipes. *Appl. Therm. Eng.* **2014**, *63*, 406–418. [[CrossRef](#)]
10. Choi, J.; Sano, W.; Zhang, W.; Lee, Y.; Borca-Tasciuc, D.A. Experimental investigation on sintered porous wicks for miniature loop heat pipe applications. *Exp. Therm. Fluid Sci.* **2013**, *51*, 271–278. [[CrossRef](#)]
11. Wang, D.; Wang, X.; Zhou, P.; Wu, Z.; Duan, B.; Wang, C. Influence of packing density on performance of porous wick for LHP. *Powder Technol.* **2014**, *258*, 6–10. [[CrossRef](#)]
12. Qu, Y.; Zhou, K.; Zhang, K.; Tian, Y. Effects of multiple sintering parameters on the thermal performance of bi-porous nickel wicks in Loop Heat Pipes. *Int. J. Heat Mass Transf.* **2016**, *99*, 638–646. [[CrossRef](#)]
13. Wang, H.; Lin, G.; Bai, L.; Fu, J.; Wen, D. Experimental study on an acetone-charged loop heat pipe with a nickel wick. *Int. J. Therm. Sci.* **2019**, *146*, 106104. [[CrossRef](#)]
14. Guo, Y.; Lin, G.; Zhang, H.; Miao, J. Investigation on thermal behaviours of a methane charged cryogenic loop heat pipe. *Energy* **2018**, *157*, 516–525. [[CrossRef](#)]
15. Guo, Y.; Lin, G.; He, J.; Bai, L.; Sun, Y.; Zhang, H.; Miao, J. Experimental analysis of operation failure for a neon cryogenic loop heat pipe. *Int. J. Heat Mass Transf.* **2019**, *138*, 96–108. [[CrossRef](#)]
16. Guo, Y.; Lin, G.; Bai, L.; Miao, J.; Peterson, G.P. Experimental study of the thermal performance of a neon cryogenic loop heat pipe. *Int. J. Heat Mass Transf.* **2018**, *120*, 1266–1274. [[CrossRef](#)]
17. Guo, Y.; Lin, G.; He, J.; Bai, L.; Zhang, H.; Miao, J. Experimental study on the supercritical startup and heat transport capability of a neon-charged cryogenic loop heat pipe. *Energy Convers. Manag.* **2017**, *134*, 178–187. [[CrossRef](#)]
18. He, J.; Guo, Y.; Zhang, H.; Miao, J.; Wang, L.; Lin, G. Design and experimental investigation of a neon cryogenic loop heat pipe. *Heat Mass Transf.* **2017**, *53*, 3229–3239. [[CrossRef](#)]
19. Guo, Y.; Lin, G.; Bai, L.; Bu, X.; Zhang, H.; He, J.; Miao, J.; Wen, D. Experimental study on the supercritical startup of cryogenic loop heat pipes with redundancy design. *Energy Convers. Manag.* **2016**, *118*, 353–363. [[CrossRef](#)]
20. German, R.M. *Sintering: From Empirical Observations to Scientific Principles*; Butterworth-Heinemann: Oxford, UK, 2014.
21. Li, X.; Yao, D.; Zuo, K.; Xia, Y.; Yin, J.; Liang, H.; Zeng, Y. Microstructure and permeability of porous YSZ ceramics fabricated by freeze casting of oil-in-water suspension. *J. Eur. Ceram. Soc.* **2020**, *40*, 5845–5851. [[CrossRef](#)]
22. Levänen, E.; Mäntylä, T. Effect of sintering temperature on functional properties of alumina membranes. *J. Eur. Ceram. Soc.* **2002**, *22*, 613–623. [[CrossRef](#)]

23. Ji, S.; Liu, Z.; Wang, G.; Liu, Y.; Jing, Y. Effects of sintering temperature and particle size on permeability of functionally gradient composite porous materials prepared by hanging slurry process. *SN Appl. Sci.* **2020**, *2*, 2046. [[CrossRef](#)]
24. Lunin, L.E.; Kostornov, A.G. Homogeneity of the porous structure of permeable powder materials in compaction and sintering. *Sov. Powder Metall. Met. Ceram.* **1992**, *31*, 1072–1074. [[CrossRef](#)]
25. Al-Qadhi, E.; Li, G.; Ni, Y. Influence of a two-stage sintering process on characteristics of porous ceramics with sewage sludge and coal ash as low-cost raw materials. *Adv. Mater. Sci. Eng.* **2019**, *2019*, 3710692. [[CrossRef](#)]
26. Vasanth, D.; Uppaluri, R.; Pugazhenthii, G. Influence of sintering temperature on the properties of porous ceramic support prepared by uniaxial dry compaction method using low-cost raw materials for membrane applications. *Sep. Sci. Technol.* **2011**, *46*, 1241–1249. [[CrossRef](#)]
27. Deutou, J.N.G.; Kamga, V.E.L.S.; Kaze, R.C.; Kamseu, E.; Sglavo, V.M. Thermal behaviour and phases evolution during the sintering of porous inorganic membranes. *J. Eur. Ceram. Soc.* **2020**, *40*, 2151–2162. [[CrossRef](#)]
28. Rockland, J.G.R. The determination of the mechanism of sintering. *Acta Metall.* **1976**, *15*, 277–286. [[CrossRef](#)]
29. Jost, W. *Diffusion in Solids, Liquids, Gases*; Academic Press: New York, NY, USA, 1952.
30. Nichols, F.A.; Mullins, W.W. Morphological changes of a surface of revolution due to capillarity-induced surface diffusion. *J. Appl. Phys.* **1965**, *36*, 1826–1835. [[CrossRef](#)]
31. Coble, R.L. Initial sintering of alumina and hematite. *J. Am. Ceram. Soc.* **1958**, *41*, 55–62. [[CrossRef](#)]
32. Kingery, W.D.; Berg, M. Study of the initial stages of sintering solids by viscous flow, evaporation-condensation, and self-diffusion. *J. Appl. Phys.* **1955**, *26*, 1205–1212. [[CrossRef](#)]
33. Jena, A.; Gupta, K. *Advanced Technology for Evaluation of Pore Structure Characteristics of Filtration Media to Optimize Their Design and Performance*; Porous Materials, Inc.: New York, NY, USA, 2003.
34. Byon, C.; Kim, S.J. Capillary performance of bi-porous sintered metal wicks. *Int. J. Heat Mass Transf.* **2012**, *55*, 4096–4103. [[CrossRef](#)]
35. Li, H.; Fang, X.; Li, G.; Zhou, G.; Tang, Y. Investigation on fabrication and capillary performance of multi-scale composite porous wick made by alloying-dealloying method. *Int. J. Heat Mass Transf.* **2018**, *127*, 145–153. [[CrossRef](#)]